nature communications

Article

https://doi.org/10.1038/s41467-025-64465-0

27%-efficiency silicon heterojunction cell with 98.6% cell-to-module ratio driving new momentum towards the 29.4% limit

Received: 17 June 2025

Accepted: 17 September 2025

Published online: 24 October 2025

Check for updates

Zhigang Xie[1] ✉, Haijiang Lu[1], Guangtao Yang[1], Zhan Gao[1], Kun Zhu[1], Yongheng Wang[1], Zibo Meng[1], Cong Guo[1], Haiyang Pei[1], Qianqian Jiang[1], Hongwei Li[1], Shu Zhang[1,2], Haiyuan Chu[1], Xue Chen[1], Yifeng Chen[1] ✉ & Jifan Gao[1] ✉

Silicon heterojunction technologies based on both-sided nanocrystalline contact layers currently offer the best passivation for commercial solar cells. We further improved this structure with rear-side polishing and progressive RF/VHF PECVD film deposition methods for doping layers, enabling high-pace mass production while maintaining notable passivation quality. Following this optimization, a certified cell efficiency above 27.0% and a fill factor of 87.06% are achieved on a large-area rectangular wafer (210 mm half-cell). With a multibusbar round-ribbon (smart-wire) design, we demonstrate a certified module efficiency of 25.44% and a module fill factor above 86% (for the first time) under a masked area of 1.63 m^2, which is on par with the current world record module efficiency typically held by back-contact cell structures. Remarkably, the high V_{OC} × FF value of 0.652–0.655 V was backed by a solid cell-to-module ratio of 98.6%. With respect to silicon single-junction solar cells, this work demonstrates significant progress toward Auger recombination dominance, a factor that is more critical than reducing front-side optical shading to approach the 29.4% efficiency limit.

Over the past two decades, the chasing of higher-performance photovoltaic devices has accelerated with a decreasing carbon footprint. Among those approaches, front-back-contact (FBC) devices are predominant. Their evolution has progressed from diffusion-based contact technologies (back surface field or BSF, passivated emitter and rear cell or PERC[1], etc.) to tunneling passivation technologies (such as tunnel oxide passivated contact or TOPCon[2]) and SHJ for reducing interface recombination. Initially, targeting a concentrator approach, SunPower, as a pioneer, started interdigitated back contact (IBC) commercialization. In 2010, SunPower took the lead in both large-area cell (24.2%) and module (21.4%)[3] performance after the integration of tunneling-based contact. In 2011, Sanyo introduced 23.7% silicon heterojunction (SHJ) technologies[4] with bifacial and ultrathin concepts at the EUPVSEC. From then on, SunPower and Sanyo/Panasonic, or IBC vs SHJ, became rivals in high-efficiency competition. In 2012, Sanyo hit a major milestone, with an SHJ efficiency of 24.7% and an open-circuit voltage (V_{OC}) above 750 mV[5,6]. For quite a long time, SunPower has been taken as the highest-efficiency module maker, and Sanyo has locked the spot of the highest-efficiency cell.

It is not unnatural to combine full passivation and all-metal back in one device. Sanyo announced their 25.6% heterojunction back contact (HBC) results[7] in the 2014 EUPVSEC. In the same section, SunPower released their 25.0% TBC cell results[8] and a series resistance (R_S) of 0.34 Ω cm^2 was achieved in this "towards the practical limits" publication. Nevertheless, Panasonic held on their 23.8% HBC module[9] ramping-up, but Kaneka continued to work on high-efficiency heterojunction-based technologies and updated their stunning results of 26.3%[10], 26.6%[11], and 26.7%[12] in a row with similar HBC structures.

[1]State Key Laboratory of PV Science and Technology, Trina Solar, ChangZhou, China. [2]College of Materials Science and Technology, Nanjing University of Aeronautics and Astronautics, Nanjing, China. ✉e-mail: zhigang.xie@trinasolar.com; yifeng.chen01@trinasolar.com; jifan.gao@trinasolar.com

Kaneka had held the record since 2016 until LONGi broke it with SHJ M6 cells in 2022[13,14]. The new record is 26.81%, with a fill factor (FF) above 86%, on the basis of the implementation of a P-side nanocrystalline silicon (ncSi) emitter. In Fig. 1a, we list the cell records from the past 15 years on the basis of data from Martin Green's *solar-cell efficiency tables* (or "Table", updated to v65[15]). FBC and BC structures have alternatively taken the lead. In principle, FBCs excel in terms of passivation (higher V_{OC} and FF), and BCs stand out in terms of the short-circuit current (J_{SC}).

Although off the record table, the Maxwell group followed this SHJ approach and was able to reproduce an M6 wafer result of 26.4% with low-cost Cu plating[16] by working with SunDrive and Indium-free TCO approaches[17]. Recently, the authors reported a cell efficiency of 26.6%, with an improved FF of 86.4%[18]. Moreover, the solar industry is moving from M2 (156 mm) and M6 (166 mm) wafering towards an even larger format between M10 (182 mm) and G12 (210 mm). Unfortunately, there was a cleaving loss of at least 0.35% (absolute, or abs), even with the "loss-free" method (Table S1 and S2). To balance wafer slicing yield and ingot growth cost, a new standard rectangular wafer (M10 half or G12 half) is on the roadmap. However, the reported cell efficiency is still at least 0.15%-0.20% (abs) lower than that of M6 results[19] because of the edge effect. Moreover, the initial results from LONGi are provided with long process time conditions and are not completely scalable. These methods are based on both-sided texturing with a surface recombination J_{01} close to 1 fA/cm^2 (a practical limit) and a noticeable J_{02} of ~0.3 nA/cm^2 (Table 2 of ref. 20). The success of SHJ mass production requires a significantly shorter reaction time (less than 180 s for each layer, etc.) achieved through fast nanocrystallization enabled by a much higher power density. Ion bombardment damage degrades surface passivation, which is only partially recoverable via light[21] or current injection[22]. The remaining interface defects necessitate further optimization through structural or process tuning. Implementing rear-side polishing significantly eases this bottleneck. With the 210 mm half-cell, we were able to produce a cell efficiency of 27.0%, with a V_{OC} of 749.2 mV and an FF of 87.06%. The results were independently verified via the ISFH CalTeC, as shown in the plot in Fig. 1b. We implemented very-high-frequency plasma-enhanced chemical vapor deposition (VHF-PECVD) on the primary doping layer. Researchers from Maxwell reported that from radio-frequency PECVD (RF-PECVD) to VHF-PECVD[16], there was a significant increase in nanocrystallization and cell performance. However, excess bombardment can produce porous structures and compromise long-term stability. By introducing a 13 MHz RF nucleation layer, damage to the intrinsic amorphous silicon (aSi) underlying layer was suppressed, and counterintuitively, fast and stable ncSi formation was observed, especially to the N-side ncSi layer.

By integrating those renovations into one state-of-the-art SHJ solution, a batch of champion modules was produced with a masked area of 1.63 m^2. The sample was transferred to the Fraunhofer ISE for certification. The best module achieved a certified efficiency of 25.44% with a certified FF of 86.03%, which is higher than the previous large-area module record, 24.9% set by Maxeon in Jan 2024[23], or 25.4% set by LONGi in July 2024[15].

Results

A rear-side polished SHJ cell

Historically, Sanyo developed the initial HIT[24] cell with a symmetrical layout. A pyramid-like surface with a (111) orientation is the basis for thin film deposition. This morphology is ideal for light harvesting but is not friendly to surface passivation, as the peak, valley, or ridge is usually the host of dangling bonds. The rear-side polishing solution was first implemented in PERC flow to eliminate counterdoping naturally and provide a clean surface for aluminum oxide passivation[25–31]. TOPCon cell flow still follows a similar logic, as the (002) surface offers

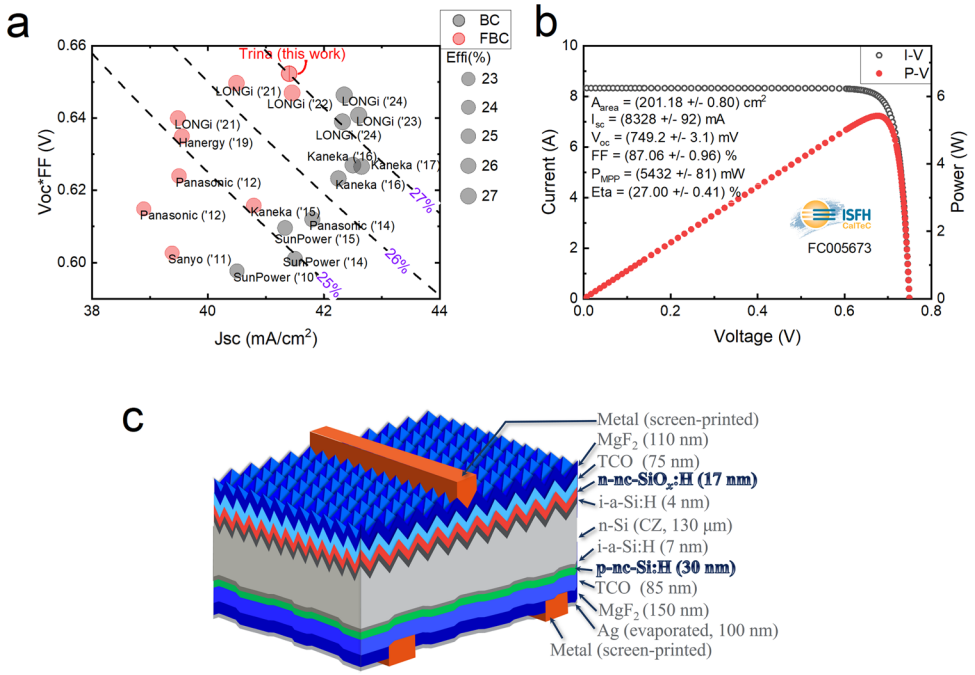

Fig. 1 | Crystalline silicon solar cell champion results and the best result in this work. a Champion cell leads composed of two groups of cell technologies: FBCs are higher on V_{OC} and FF because of full face passivated contact but lower on J_{SC}, primarily because of front-side shading from fingers and busbars; BCs excel in monofacial efficiency measurement but typically run low on FF because of excessive processing steps. All the cell records come from Martin A. Green's "Table" (from v30 to v65), with the exception of the work discussed in this paper. **b** Our recent SHJ (an FBC cell) result verified by ISFH CalTec. The measurement is based on an apertured (ap) calibration practice to eliminate edge effects, which is typical for rectangular half-cells. The wafer thickness is 140 µm, and the front side H-pattern has an 18-busbar design. **c** The reported cell has a monofacial design with a magnesium fluoride (MgF_2) antireflection layer at the front and MgF_2/silver film stacks at the rear side. More importantly, we have a rear-side-polished structure to further improve the surface passivation. The film thickness reported is for the textured surface (front) and polished surface (back). TCO refers to transparent conductive oxide films.

a lower density of defect states (D_{it}) at the silicon/oxide interface. All-back-contact cells also have a significant percentage of polished rear surfaces.

We used silicon nitride (SiNx) as a protective mask. During the adjusted saw damage etching, the polished surface evolves from (111) crystallographic dominated conditions quickly into mixed facets with (211) and (311), and finally transitions into a combination of surface slopes between (311) and (411). The wet chemistry and optical characterization are described in refs. 32,33. Here, we define the characteristic angle as the angle between tilted facets and the crystallographic (002) plane. The perfect pyramid facets should have a theoretical value of 54.7°, whereas (311) should have an angle of 25.2°, and (411) should have an angle of 19.5°. We further define a planar fraction f_p, as the ratio of the area of the planar surface to the total area projection into the (002) substrate.

In our experiments, the alkaline solution was prepared at a 6% concentration by weight (wt%) and stabilized at 70 °C. The samples were processed with increasing time from 30 s to 50 s to 260 s. We observed a quick increase in f_p from 35% to a saturated value above 90%. In lieu of our optimized SHJ processes, the cells were finally measured with a Sinton FCT-650 IV tester, including a pseudo-FF (pFF). The PECVD recipe was adjusted to cater to the difference in surface ratios. However, one finalized recipe was applied across this designed experiment, so the passivation is under performance for the conditions with lower f_p. The cell passivation is saturated when the polishing time exceeds 80 s, but the cell performance further peaks at 110 s. We did not observe a J_{sc} increase compared with that of the backside polished PERC cells, and the majority of the enhancement is related to passivation (J_0, pFF, etc.). Moreover, we also observed an improvement in Rs after this baseline migrated, even with our double-sided ncSi contacts. The cells were further characterized via high-resolution transmission electron microscopy (HRTEM). In Fig. 2c, on the textured surface, there is abundant ncSi formation, but with a smaller size and isolated distribution. As a comparison, in Fig. 2d, on the shallow slope facet and planar area, the ncSi formation is significantly enhanced, typically extending across the entire layer as columnar structures. Nevertheless, the improvement in passivation should come from the planarized back-side surface itself.

Progressive RF/VHF PECVD ncSi process

With the implementation of both sides of the ncSi contact layer, it is relatively straightforward to achieve a J_{01} close to 1 fA/cm^2. However, in seeking transferable technology, we must handle the tact time concern by utilizing high-power-density VHF to foster ncSi formation with a deposition rate of at least 1–2 Å/s. Before the main step of the ncSi layer, an incubation layer is typically necessary[34–37], and this layer is crucial for the passivation quality.

Raman spectroscopy with a confocal microscope setup was utilized for monitoring ncSi growth[38,39]. On the basis of the literature[40], the ncSi signal peaks at a Raman shift of 510–520 cm^{-1}, which is related to a transverse optical phonon branch (TO_2), whereas the aSi signal peaks at 480 cm^{-1} (TO_1). On the red side of TO_2, asymmetrical broadening is typically observed, possibly due to a transition from aSi to ncSi states. In Fig. 3d, a typical Raman measurement result is displayed with 3 Gaussian peaks successfully deconvoluted in the order of I_1, I_{2b}, and I_2. The crystallinity ratio X_c is defined as:

$$x_c = \frac{I_{2b} + I_2}{I_1 + I_{2b} + I_2} \tag{1}$$

The window layer, a phosphor-doped ncSi film, is codoped with carbon dioxide (CO_2) for a tradeoff between transparency and contact resistance. In Fig. 3a, we define an oxygen ratio on the basis of the ratio of CO_2/SiH_4 and observe the impact on X_c. With increasing oxygen ratio, X_c clearly decreases (as shown in the summary plot of Fig. 3c), whereas the TO_2 peak clearly broadens. An 80% oxygen ratio is optimal for optical engineering, but it delivers a significantly lower X_c of 30–35%. We propose a progressive transition from the RF PECVD process to the VHF bulk layer. After performing similar oxygen mapping, we find that it offers a higher crystallinity ratio overall. The cell *I–V* measurements suggest improved passivation, with evidence of increased V_{OC} and pFF. At an 80% oxygen ratio, the crystallinity ratio is in the range of 40–45%. The success of this progressive scheme suggests a possible mechanism: RF plasma is ideal for nucleation, but VHF plasma is preferred for fast and efficient nano-crystallization. The resistive incubation layer itself possibly serves as a barrier to screen out the excessive bombardment.

We deliver a similar solution to the boron-doped emitter layer. Although we did not observe a change in X_c (fluctuating at approximately 60–65%), a passivation improvement without compromising Rs was confirmed. The results are shown in Fig. 3e.

Inside an n-type silicon device, the typical recombination loss can be defined as:

$$J_{rec} = J_{02}\exp\left(\frac{eV}{2kT}\right) + q \cdot W \cdot \frac{p}{\tau} + J_{01}\exp\left(\frac{eV}{kT}\right) + q \cdot W \cdot C_{Auger}\left(n^2 p + np^2\right) \tag{2}$$

Under carrier confinement,

$$np = {n_i}^2 \exp\left(\frac{eV}{kT}\right) \tag{3}$$

The first 3 terms of Eq. (2) originate from the Shockley–Read–Hall (SRH) recombination after the surface defect level is included in the picture. The variables and constants are explained in detail in the Methods section. Among diffusion-based cell technologies, such as PERC and TOPCon, only the 2nd term and 3rd term dominate minority carrier lifetime measurements. The last term of Eq. (2) is derived from Auger recombination. With the optimized wafer quality (τ ~ 15 ms) and surface passivation, this loss begins to dominate, and the ideality factor (n) of the I–V curve approaches 2/3. This is the basis of ultrahigh FF and pFF, which are typically only associated with SHJ devices.

However, in the earlier days of SHJ development, substantial parasitic loss is attributed to J_{02}. The IP-side interface is prone to situations in which electrons and holes have close populations. Even within the work related to the phenomenal breakthrough of 26.81%, there was a loss of J_{02} ~ 0.3 nA/cm^2 witnessed by a clear slope when the injection level of the minority carrier density (MCD) was scanned from 1×10^{14}/cm^3 (low injection) to 1×10^{15}/cm^3 (median injection) (Fig. 4c of Ref. 13).

We use a Sinton WCT-120[41–44] to evaluate the minority carrier lifetime (MCL) performance. Given the typical wafer thickness of 120–140 μm, our best conditions offer a measured MCL of 12 ms (from low to median injection) and over 5 ms for MCD at 1×10^{16}/cm^3 (high injection). This gives an overall J_{01} as low as 1.06 fA/cm^2, as shown in Fig. 3f. Additionally, this is the first study in which a "clean" and flat MCL response across the low to median injection range has been published for all types of silicon solar cells, including BCs.

A large-area SHJ module based on optimized front–back contact cells

While it is not trivial to determine the true cell performance, especially on the FF side, we propose a large area module comparison as a cross-check. For this purpose, the best three modules were sent to Fraunhofer ISE and were all reported to have a module efficiency of 25.4%, including a champion at 25.44%. Within a similar time frame as the module measurement of 25.4% by Fraunhofer ISE, LONGi's champion

https://doi.org/10.1038/s41467-025-64465-0

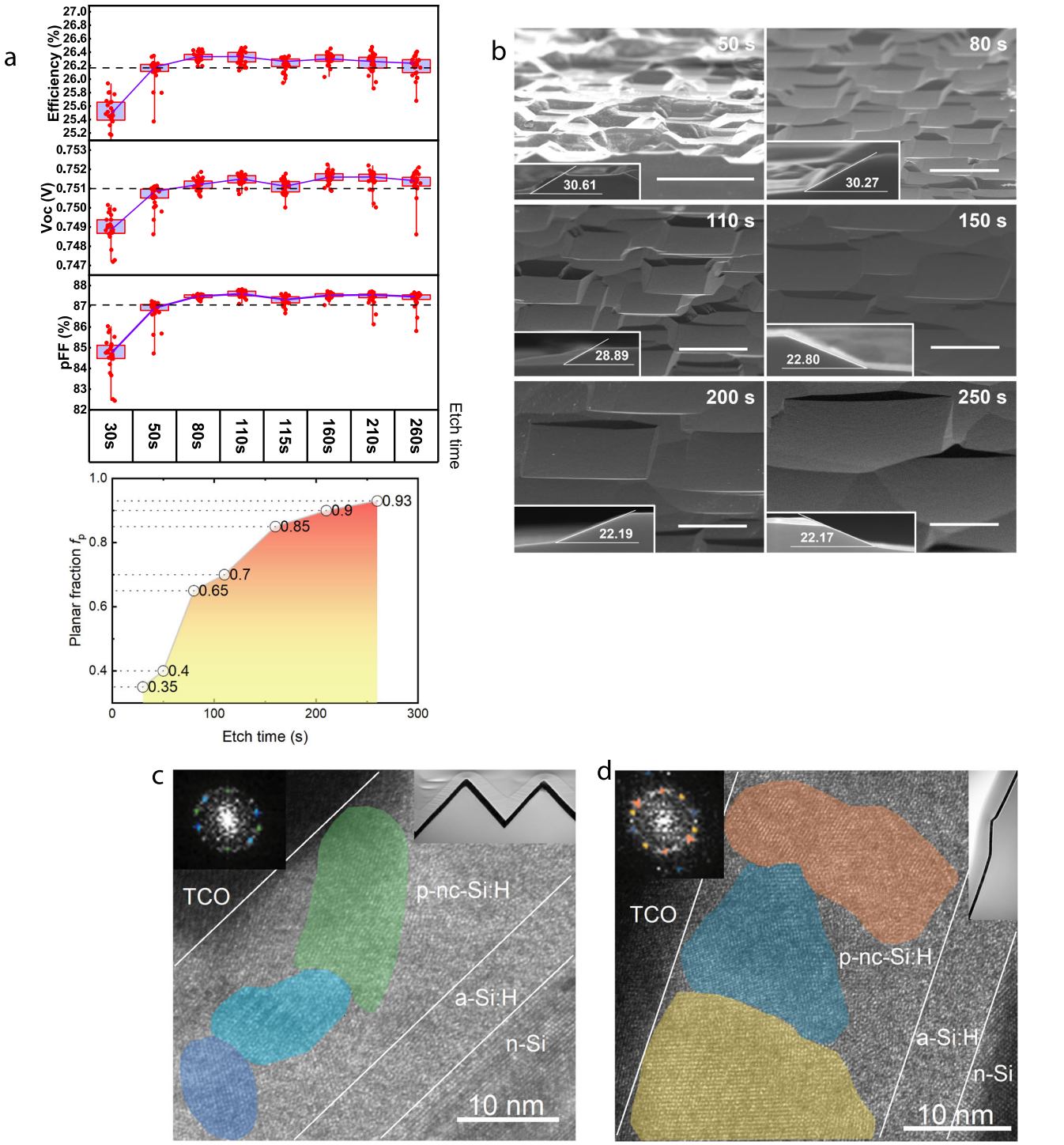

Fig. 2 | Rear side polished SHJ process. Both-sides-textured wafers were coated with SiN_x film from a tube furnace. This step was followed by rear-side polishing with alkaline-based recipe (70 °C and 6 wt% KOH solution). The etch time is increased from 30 s to 260 s. **a** SHJ cells with different rear polishing time are processed and measured. In particular, the cell efficiency (Effi), V_{OC}, and pFF are shown as boxplots with median values connected to highlight the trend. The upper and lower limits of the box plot refer to the 25th percentile and 75th percentile, respectively. The planar faction f_p changes accordingly. **b** SEM images from the side view (inserts) and tilted view (rear polishing time of 50 s, 80 s, 110 s, 150 s, 200 s, and 250 s). All scale bars are 5 μm. **c**, **d** High-resolution cross-section TEM images of a regular textured sample (**c**) and a group with rear polishing time of 80 s (**d**). The typical facets from the left cells (**c**) are standard (111) facets, but (311) or (411) facets for the right cell (**d**).

cell from the same cell technology was also measured at ISFH, with a result of 27.4%[15].

While the method of FBC cell calibration (measured with front jigs and backside full-area contact) is technically proven, BC cells must be tested with customer-provided chucks after a qualification process. However, the certified results, especially those of FF, still depend on the chuck design. On the other hand, large area module certification is a more representative reference. From Table 1, we list the champion module records for the past 15 years starting from SunPower's TBC results, which are based on Martin Green's "Table" updated biannually.

https://doi.org/10.1038/s41467-025-64465-0

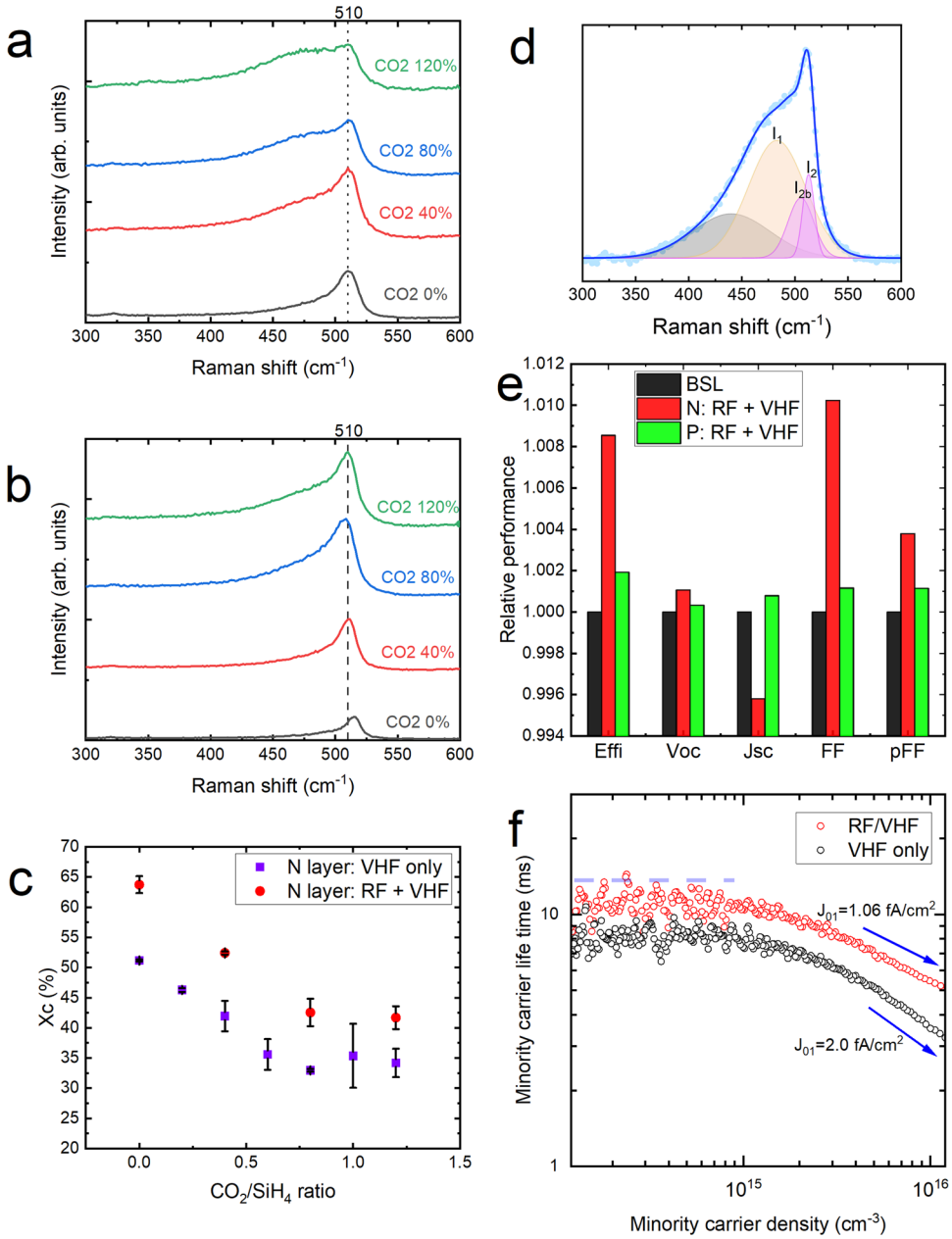

Fig. 3 | PECVD process improvement from a progressive RF/VHF approach. **a** Raman spectroscopy results of a pure VHF n-type ncSi film on top of low-iron glass. The probe beam is from a 325 nm laser to obtain a reasonable penetration depth to cover both the intrinsic aSi film and the complete stack of the n-type ncSi film. A response of the crystallinity ratio X_c to CO_2 doping is observed. **b** Raman spectroscopy results for a progressive RF/VHF n-type ncSi film. The incubation layer starts with the RF process, and the majority of the ncSi bulk layer is accomplished with the VHF process, including the contact layer. The response of the crystallinity ratio X_c to CO_2 doping is repeated for this batch of samples. **c** An overlay of two crystallinity ratio vs CO_2 doping curves. The error bars are calculated from the standard deviations of the measurements. **d** A typical Raman spectroscopy curve was successfully deconvoluted. The peak close to 440 cm^{-1} should be related to amorphous silicon with oxygen incorporation and was not included in the X_c calculation. **e** Comparison of the performance ratios (Effi, V_{OC}, J_{SC}, and FF). The baseline process is defined to have a performance ratio of 1. This progressive RF/VHF optimization is applied to both n-type and p-type ncSi contact layers. The benefit is more outstanding for the n-type layer, but an improvement in passivation also occurs at the p-side. **f** Minority carrier lifetimes are measured for both samples with a Sinton WCT-120. Given that the bulk lifetime can reach 15 ms, the minority lifetime measured at an injection level of $1 \times 10^{15}/cm^3$ is improved from 8 ms to 12 ms, whereas at an injection level of $1 \times 10^{16}/cm^3$, the improvement is from 3.3 ms to 5 ms.

To further breakdown the cell-to-module (CTM) components, we name a defined CTM, as well as the normalized J_{SC} and V_{OC} for clarification (details in the Methods section). From this table, most of the champion modules are from BC technologies. However, the best results for FF are still approximately 83–84%.

In our case, with smart-wire technology[45–47], the additional optical shading is only 1.1% (from 28 round ribbons with a diameter of 250 μm) after excluding the existing busbar shading. We have improved our engineering work, and the details are discussed in Ref. 48. Furthermore, the optical loss is improved via narrow overlap between neighbouring cells, which is straightforward for FBC structures[49,50] but technically challenging for BC cells[51].

To elaborate on the CTM differences between the FBC and BC modules, we compared recent state-of-the-art technologies from both sides. For FBC, the SHJ cell (27.0% efficiency) and corresponding module (25.44% efficiency) were designated as the FBC-cell and FBC-

https://doi.org/10.1038/s41467-025-64465-0

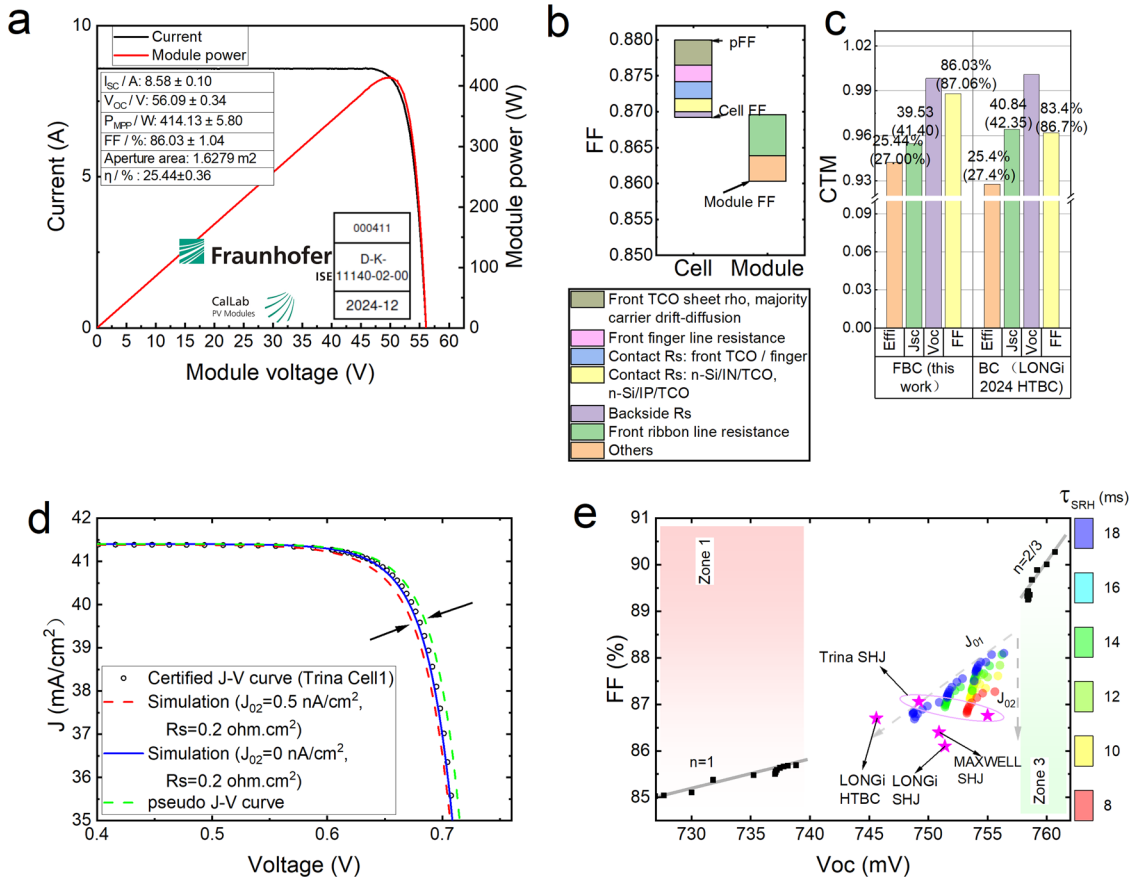

Fig. 4 | The champion module results and related cell-to-module loss analysis. **a** The certified result from Fraunhofer ISE. The module has 75 units of FBC cells in total with smart-wire zero-busbar interconnections as the stringing technology. **b** Cell-to-module loss analysis, especially for series resistance and FF. The top three loss terms are from majority carrier lateral spreading (TCO resistivity and carrier drift–diffusion), front-side TCO–Ag contact R_C (~0.8 mΩ cm^2) and front-finger line resistance. The front-finger line resistance loss at the cell side is estimated on the basis of an 18 BB assumption at the cell side, but a 28 BB configuration at the module side. The series resistance loss from the front-side ribbon is based on a round cross-section with a 220-μm-diameter inner core. There is other Rs loss from the backside ribbon, end connection and short cabling. **c** The specially defined CTM loss from the champion cell to the champion module. The FBC data are based on this work, but the BC data come from Martin A. Green's "Table" (v 65). **d** Comparison of the certified cell results with the parametric modelling results: pseudo *J*–*V* with the assumption of τ_{SRH} = 15 ms, J_{01} = 1 fA/cm^2, and J_{02} = 0 nA/cm^2; a simulated *J*-*V* with an R_S of 0.2 Ω cm^2 added to the pseudo *J*–*V* curve; and a *J*–*V* curve with an additional J_{02} = 0.5 nA/cm^2 recombination source. All the modelling is based on a wafer thickness of 130 μm and resistivity of 1.5 Ω cm. **e** pFF (or FF_0) versus V_{OC} curve. In the regime dominated by surface recombination J_{01} (Zone 1), the ideality factor n of the *I*–*V* curve approaches 1, and V_{OC} is typically less than 740 mV. In Zone 3, when both surface recombination terms diminish and τ_{SRH} approaches infinity, pFF quickly climbs up in this Auger-recombination-dominated regime. In this situation, the ideality factor is close to 2/3. In the interim, around the vicinity of V_{OC} = 750 mV, the upper limit of pFF also ramps up quickly, with fast reductions in both J_{01} and J_{02}.

Table 1 | The historical champion data on the large-area module (with an aperture area above 1 m^2)

Record	Effi %	Area m^2	V_{oc} mV	J_{sc} (mA/cm^2)	FF %	Test centre (date)	Description
1	21.4 ± 0.6	1.578(ap)	714.6	38.28	78.4	NREL (Oct 2009)	SunPower (TBC 96 cells)
2	22.4 ± 0.6	1.5775(ap)	724.7	38.59	80.1	NREL (Aug 2012)	SunPower (TBC 96 cells)
3	22.8 ± 0.6	1.57389(ap)	722.5	39.4	80	NREL (Jun 2015)	SunPower (TBC 96 cells)
4	23.8 ± 0.5	1.1562(ap)	741.7	39.36	81.6	AIST (Jan 2016)	Panasonic (HBC 72 cells)
5	24.4 ± 0.5	1.3177(ap)	736.1	41.31	80.1	AIST (Sep 2016)	Kaneka (HBC 108 cells)
6	24.7 ± 0.3	1.7806(ap)	741.4	40.16	82.9	NREL (April 2023)	Maxeon (TBC 112 cells)
7	24.9 ± 0.3	1.7753(ap)	741.8	40.46	82.8	NREL (Jan 2024)	Maxeon (TBC 112 cells)
8	25.4 ± 0.3	1.8342(ap)	746.3	40.84	83.4	FhG-ISE (July 2024)	LONGi (HTBC 108 cells)
9	25.44 ± 0.36	1.6279(ap)	747.9	39.53	86.03	FhG-ISE (Nov 2024)	This work (SHJ 75 cells)

The normalized V_{OC} and J_{SC} values are extracted for the convenience of the cell-to-module CTM calculation. From Records 1 to 9, the data for sourcing come from Martin Green's "Table" (versions 39, 42, 47, 48, 49, 62, 63, 64, and 65, respectively). The LONGi module based on HTBC was measured at the ISE, not by the NREL, as previously reported.

Table 2 | The recent top certified cell results

Cell name	Effi %	V_{OC} mV	FF %	J_{SC} mA/cm²	V_{OC} x FF V	Data Source
Trina SHJ cell1	27.00	749.2	87.06	41.4	0.652	This work
Trina SHJ cell2	27.08	755.0	86.76	41.34	0.655	This work
LONGi SHJ	26.81	751.4	86.1	41.45	0.647	Nature energy 8, 789 (2023)
Maxwell SHJ	26.6	750.9	86.4	41	0.649	ACS energy letters 10, 2503 (2025)
LONGi HTBC	27.4	745.6	86.7	42.35	0.646	Ref. 23

The top cell results listed in this table are marked and refer to this threshold of the FF plot in Fig. 4e. All test results are certified by the ISFH. In the table, a V_{OC} × FF value is calculated, where "M" denotes the value of V_{OC} × FF at the module side.

module, respectively. For BC, LONGi's heterojunction back-contact (HTBC) technology served as the ref. 15 and was named accordingly. Figure 4c shows that there is a 1.87 mA/cm² decrease in the J_{sc} from the FBC-cell to the FBC-module. The loss is 1.5 mA/cm² for the BC case. The overall CTM of FBC technology is 94.2%. We must clarify that this defined CTM differs from the conventional power loss CTM, where the sourcing cells exhibit a typical efficiency deficit of 0.5% (abs). Additionally, SHJ cells benefit from light injection, which disappears after preconditioning. Furthermore, 1 ~ 1.5% of the gap area is still ineffective even after tight alignment is achieved. Overall, the conventional CTM will still be approximately 98.5%.

However, on the BC side, the defined CTM is only 92.7%, and the majority of the loss comes from FF (from 86.7% of the BC-cell to 83.4% of the BC-module). The simulation confirms that in the FBC case, the ohmic loss from the front side ribbon is only 0.6%. The remaining details regarding the overall Rs are further categorized in Fig. 4b. At this moment, the most perfect passivation still aligns with the FBC cell and supports a pFF of ~88.0% to start with. To determine the contact resistance R_C of both n-Si/IP/TCO and n-Si/IN/TCO, we followed the method in Refs. 52–55 and concluded that the combination of contact resistance R_C from both surfaces is close to 35 mΩ·cm². The overall R_S of our champion result is close to 205 mΩ·cm². To pursue champion module results, there are common practices, including wider ribbons applied to the rear side. For BC modules, the all-contact-back structure should be favoured even more, unconcerned with front-side obstructions. Therefore, the discrepancy points to the FF determination on the cell side.

A CTM of V_{OC} × FF itself also provides insight. This CTM of only 96.3% makes the high-efficiency report from HTBC questionable. On the other hand, the solid backup from the CTM of 98.3–98.6% validates the high V_{OC} × FF of 0.652–0.655 V for our SHJ FBC cells. Recently[56], LONGi has improved the HTBC technology in terms of both cell efficiency (with an efficiency of 27.81% and FF of 87.5%) and module efficiency (with an efficiency of 25.96% and FF of 84.0%). However, this defined CTM of V_{OC} × FF is still approximately 96.4%.

Discussion

We have achieved near-perfect passivation (J_{01} = 1.06 fA/cm², J_{02} ~ 0 nA/cm² and pFF of 88.0%) and the lowest series resistance (~0.2 Ω cm²) on the same SHJ FBC cell. This offers a solid basis for identifying a new FBC cell record of 27.0%, with a final FF of 87.06%. The power loss is clearly categorized and partitioned. This notable result is further justified by a certified module result of 25.44%, with a final FF above 86%. Although FBC products intuitively have a disadvantage in terms of current due to shading loss, the built-in advantage of FF from both passivation (pFF) and full-area contact (Rs) pushes the device to reach a practical higher limit. On the other hand, pinhole defects from excessive processes, as well as isolation trenches between the P and N regions, result in a tremendous J_{02} loss term (~1 nA/cm²), which limits the pFF for BC structures.

In Fig. 4e, an intrinsic limitation of FF is calculated on the basis of a variation in cell parameters, including the wafer resistivity, τ_{SRH}, and surface recombination terms of J_{01} and J_{02}. In the surface-recombination dominated regime (Zone 1), Voc is typically under 740 mV, and the internal cap on pFF is ~85%. On the opposite side (Zone 3), if both surface terms of J_{01} and J_{02} are diminished, plus a superhigh-quality wafer (with a τ_{SRH} of ~100 ms), the solar cell will experience an Auger-recombination dominated regime, and another 5 ~ 6% gain in V_{OC} × FF is possible. In the interim regime, the SHJ demonstrates the lowest possible J_{01} ~1 fA/cm². Furthermore, our work is the only one that eliminates J_{02} completely. In Table 2, we summarize the most recent top-performing cell results for direct comparison with our work. In addition to the IP-side interface from SHJ passivation, pinhole defects in the N-poly from chemical etching, laser ablation, or insufficient phosphor doping at the interface are likely sources of climbing J_{02} defects. In the case of the HTBC cell record, with a V_{OC} of less than 746 mV, the measured FF already exceeds the allowable limit for pFF.

There is proven loss away from external shading, and a current loss of 2.5% at the cell level or 3.5% at the module level is observed. However, to approach the efficiency limit of 29.4% for single-junction silicon solar cells, the FBC structure with the best passivation will likely be the final winner. Among all those engineering designs, thin wafers with new light-trapping have more room to reach the Shockley–Queisser limit on V_{OC} × FF. Additionally, FBCs have more room for surface structure engineering, and optical loss can be overcome by light-converting particles or films. The busbar/ribbon shading can be minimized from the triangular cross-section design to handle the additional CTM loss on J_{SC}, which justifies a module efficiency of 25.8% following this work. Furthermore, we foresee a cell efficiency of over 28.4% and a large-area module efficiency of over 27% in the very near future.

Methods

Cell and module fabrication

The ingots used in this work were from the Trina Qinghai ingot and wafering division, with a tail resistivity of 1.17 Ω cm and an end resistivity of 1.05 Ω cm. The oxygen content was controlled to be less than 12 PPM, and the carbon content was measured at 0.02 PPM. The rectangular wafers (210 mm half-cell) were obtained via diamond-cut wafer slicing from a trunk with a cross-section of 210.1 × 211.6 mm. The specificity of the guaranteed intrinsic lifetime is 8 ms. An initial wafer thickness in the range of 140–160 μm was confirmed from weight measurements. After the samples were subjected to saw damage etching and random texturing, the wafers were subjected to RCA cleaning, a diluted HF dip, and hot-air drying.

For the process of rear-side polishing, 2 separate wet cleanings were applied before and after silicon nitride tube-furnace PECVD deposition. An industrial standard capacitance-coupled PECVD system was implemented for intrinsic i-a-Si:H film deposition, nanocrystalline n-nc-SiO_x:H deposition, and p-nc-Si:H deposition. The system was equipped with a multi-chamber configuration (an out-gassing and preheating chamber, an RF chamber, and a VHF doping chamber in serial connection without vacuum breaks). The intrinsic i-a-Si:H is optimized with carbon dioxide (CO_2) for enhanced transparency and passivation. For the nano-crystalline film deposition, the process

conditions include a pressure setting of 300–400 Pa, a temperature setting in the range of 160–200 °C, and a growth rate close to 1.2 Å/s. The incubation layer was prepared with a low growth rate of 0.2–0.4 Å/s. The TCO films on both sides were deposited via a reactive plasma deposition (RPD) tool with a designed target tablet from cerium-doped indium oxide (ICeO). The metallization agent was prepared through node-free stencil screen printing with a grid width of 21 μm and a height of 15 μm, as confirmed by a Zeta 3D optical microscope. The overall front side shading is approximately 2%, with an 18BB busbar structure for cell calibration at the ISFH. For the cells sent for module fabrication, a similar process with a busbar-free layout is implemented with a regular 18BB witness cell to monitor the quality and process fluctuations.

Integrated film covering (IFC) technology was adopted for interconnect techniques in our module. The IFC-based 0BB process starts by positioning the ribbon onto the carrier film, followed by arranging the cells on top of this preformed structure. The carrier film is slightly melted at approximately 100 °C to create adhesion. A final lamination occurs at a low temperature of 150 °C for 20 minutes to enable alloying between the ribbon and silver paste. To obtain an overlap of 1–1.5 mm between cells, a deformed section is created on those round ribbons.

Measurement and characterization

The lifetime post-CVD passivation was characterized by a Sinton WCT-120 tool. A standard transient photo-conductance decay technique was applied to obtain the inverse lifetime versus carrier density curve (Fig. S1). After Auger recombination is deducted, the interception is typically related to the bulk lifetime, and the slope is proportional to the J_{01} or surface recombination velocity. This methodology is valid only when the excellent passivation effects eliminate J_{02} completely and when there is only $n = 1$ surface-oriented recombination (ideality factor close to 1). For a BC structure or nonideal situation, a more detailed model (Eq. 2) is necessary to explore the devices accurately.

For the finished cells, the in-house measurement was run on a Sinton FCT-650 instrument, including one sun light IV and Suns-Voc. The nonuniformity and temperature stability satisfy the Class A requirement over an area of 210 mm × 210 mm. Although by default a voltage modulation is implemented to neutralize the capacitance effect from a high-efficiency cell, we ran a full I–V scan instead of hunt mode for all the cell tests discussed in this work. The setup itself has 12BB contact jigs on the front and full metal back chuck. We determined the series resistance adjustment to FF based on the golden sample from the ISFH calibration. For the best cell results, we sent the cells to ISFH CalTec for I–V characterization, including the spectrum response (SR). The cells were contacted at the front with elastic contact bars made of gold-coated metal foil to eliminate contact Rs, and a full area of contact was reached at the back. During this calibration process, EQE curves were also measured (Fig. S2).

For the top module certificates, we sent 3 pieces from the same batch to Fraunhofer ISE CalLab. For this purpose, we laminated a 75-cell module in a frame with a size of 1762 mm × 1134 mm. The ineffective area was taped out with a center masked area of 1.6279 m^2. Owing to customer clearance and queues, there is a 1-month gap from production to the calibration test. The module IVs were collected on an FL3-PasanHighLIGHT VLMT system, and the measurement was performed after standard preconditioning for 30 h under an irradiance of 1000 W/cm^2 with a temperature of up to 70 °C.

In particular, we screen our nano-crystalline samples via HORIBA Raman spectroscopy (model: LabRam Odyssey), and the probe beam is from a 325 nm laser for enough sampling depth into the entire contact layer. The films are prepared on a glass substrate, and the nanocrystalline contact layer is typically coated on top of the intrinsic amorphous film. We prepared the film stack exactly in the way of running film deposition on a regular functioning cell. However, there is a subtle difference between polished samples and textured wafers, and the conclusions should be carefully examined.

Device simulation

We run module-level simulations from Griddler[50,57] and cell-level simulations from Quokka[58,59].

We confirmed the electrical performance of the device from Quakka 2, which is based on the MATLAB running environment. The results are confirmed with PC2D with a customer modification to a grid size of 600 units. The surface recombination current $J_{01,}$ was from the Sinton lifetime curve, as was the bulk lifetime. In our characterization, front-side finger resistance loss is determined from line resistance measurements, and TCO/finger contact Rs is extrapolated from transfer line method (TLM) measurements[60]. The primary electrical loss is from current lateral spreading loss (from the limited conductivity of the front TCO and carrier drift–diffusion), front–line resistance, and front–line contact R_C. Owing to the full-area contact of the FBC structure, the contact Rs from both interfaces (n-Si/IP/TCO and n-Si/IN/TCO) is relatively low, as determined from separate offline measurements.

The cell-to-module loss is analysed primarily via Griddler 2.5, which also relies on a MATLAB running environment. After an FEM analysis based on the geometric and finger design profile, additional module fabrication details, such as front and rear line shapes, were added to the model. A quick simulation provides details, including the full IV and extrapolated R_S.

CTM definition

First, we obtain a normalized cell area by dividing the aperture area (1.63 m^2 in our case) by the number of cells in the serial connection (75 in our case). Then, we obtain a normalized J_{SC} from the ratio of the certified I_{SC} to the normalized cell area. The normalized V_{OC} is achieved from the ratio of the certified module V_{OC} to the number of cells in the serial connection. The value of the normalized J_{SC} is typically underrated because of the small gap between cells or strings.

The conventional CTM is defined as the ratio between the measured module power and the total power of all source cells. We further introduce a defined CTM, which is the ratio of the area efficiency of the champion module to the champion cell efficiency.

The primary gap between the conventional CTM and this defined CTM is the way to extrapolate J_{SC}, as the champion cell report typically includes a redundant antireflection coating (MgF_2, etc.). For this reason, we further define a CTM of $V_{OC} \times FF$ for standalone clarification.

Shockley–Read–Hall (SRH) recombination

The SRH expression[61] for general trap-assisted recombination is applicable to both surface defects and bulk defects:

$$R = \frac{np}{\tau_n(p + p_t) + \tau_p(n + n_t)}$$

where the average lifetimes for electrons and holes are defined as τ_n and τ_p, respectively.

Case 1. In areas where space-charge recombination is dominant, such as the n-i-p junction area, electrons and holes have very close populations, and SRH recombination can be simplified in the following way:

$$n \approx p = n_i \exp\left(\frac{eV}{2kT}\right) \Rightarrow R = \frac{np}{\left(\tau_n + \tau_p\right)p} = \frac{n_i}{\tau_n + \tau_p} \exp\left(\frac{eV}{2kT}\right) \propto J_{02} \exp\left(\frac{eV}{2kT}\right)$$

Case 2. Within the N-type silicon bulk, for a low-resistivity wafer (1.5 Ω cm), SRH recombination can be expressed as:

$$n = p + N_D, p \ll N_D \Rightarrow R \approx \frac{np}{\tau_p n} = \frac{p}{\tau_p} \; under\; confinement\; p(p+N_D) = n_i^2 \exp\left(\frac{eV}{kT}\right)$$

where N_D is the intrinsic doping of the silicon substrate.

Case 3. In the heavily doped surface area, SRH recombination can be simplified as:

$$R = \frac{pN_D}{\tau_p N_D} = \frac{p}{\tau_p} = \frac{n_i^2}{\tau_p N_D} exp\left(\frac{eV}{kT}\right) \propto J_{01} \exp\left(\frac{eV}{kT}\right)$$

Inside an n-type crystalline silicon device, together with Auger recombination, the typical recombination loss can be defined as:

$$J_{rec} = J_{02} \exp\left(\frac{eV}{2kT}\right) + q \cdot W \cdot \frac{p}{\tau} + J_{01} \exp\left(\frac{eV}{kT}\right) + q \cdot W \cdot C_{Auger}\left(n^2 p + np^2\right) \quad (4)$$

Under confinement,

$$np = {n_i}^2 \exp\left(\frac{eV}{kT}\right) \quad (5)$$

The first 3 terms of Eq. 2 comes from Shockley–Read–Hall (SRH) recombination by including the surface defect level in the picture. n and p represent the electron and hole concentrations, respectively, and V refers to quasi-Femi-level separation. n_i refers to the intrinsic carrier concentration under thermal equilibrium. τ or τ_{SRH} refers to the bulk lifetime. The other parameters are q for the electron charge and W for the wafer thickness. The 1st and 3rd terms are related to surface recombination, and the other terms are proportional to the wafer thickness W.

A general algorithm to extrapolate J_{01} and J_{02} in MCL measurements

With a Sinton MCL measurement, a set of effective minority-carrier lifetimes (τ_{eff}) is measured at an injection level ranging from 1×10^{13}/cm^3 to 3×10^{16}/cm^3. On the basis of Eq. (2),

$$J_{rec} = q \cdot W \cdot \frac{p}{\tau_{eff}} = J_{02} \exp\left(\frac{eV}{2kT}\right) + q \cdot W \cdot \frac{p}{\tau} + J_{01} \exp\left(\frac{eV}{kT}\right) + q \cdot W \cdot C_{Auger}\left(n^2 p + np^2\right)$$

In combination with the carrier confinement $p(p+N_D) = n_i^2 \exp(\frac{eV}{kT})$,

$$\frac{1}{\tau_{eff}} = \frac{1}{qWn_i}\sqrt{1+\frac{N_D}{p}} \cdot J_{02} + \frac{1}{\tau} + \frac{N_D}{qWn_i^2}\left(1+\frac{p}{N_D}\right) \cdot J_{01} + C_{Auger}\left((p+N_D)^2 + (p+N_D)p\right)$$

After further deducting the Auger recombination-related contribution, we obtain the following expression:

$$\widetilde{R} = \widetilde{M} \times \widetilde{J}$$

$$\widetilde{R} = \begin{bmatrix} (\frac{1}{\tau_{eff}})_1 \\ (\frac{1}{\tau_{eff}})_2 \\ \vdots \\ (\frac{1}{\tau_{eff}})_j \end{bmatrix} \quad \widetilde{M} = \begin{bmatrix} \frac{1}{qWn_i}\sqrt{1+\frac{N_D}{p_1}} & 1 & \frac{N_D}{qWn_i^2}(1+\frac{p_1}{N_D}) \\ \frac{1}{qWn_i}\sqrt{1+\frac{N_D}{p_2}} & 1 & \frac{N_D}{qWn_i^2}(1+\frac{p_2}{N_D}) \\ \vdots & & \vdots \; \vdots \\ \frac{1}{qWn_i}\sqrt{1+\frac{N_D}{p_j}} & 1 & \frac{N_D}{qWn_i^2}(1+\frac{p_j}{N_D}) \end{bmatrix} \quad \widetilde{J} = \begin{bmatrix} J_{02} \\ \frac{1}{\tau} \\ J_{01} \end{bmatrix}$$

Taking advantage of Excel matrix functions (such as "MMULT", "TRANSPOSE" and "MINVERSE"), we can calculate the following solution:

$$\widetilde{J} = (\widetilde{M}^T \widetilde{M})^{-1} \widetilde{M}^T \widetilde{R}$$

Reporting summary

Further information on research design is available in the Nature Portfolio Reporting Summary linked to this article.

Data availability

The source data files are provided within the supplementary document. Source data are provided with this paper.

References

1. Green, M. A. The Passivated Emitter and Rear Cell (PERC): from conception to mass production. *Sol. Energy Mater. Sol. Cells* **143**, 190–197 (2015).
2. Feldmann, F., Bivour, M., Reichel, C., Hermle, M. & Glunz, S. W. Passivated rear contacts for high-efficiency n-type Si solar cells providing high interface passivation quality and excellent transport characteristics. *Sol. Energy Mater. Sol. Cells* **120**, 270–274 (2014).
3. Green, M. A., Emery, K., Hishikawa, Y., Warta, W. & Dunlop, D. Solar cell efficiency tables (version 39). *Prog. Photovolt Res. Appl.* **20**, 12–20 (2012).
4. Kinoshita, T. et al. The approaches for high efficiency HIT solar cell with very thin (<100 μm) silicon wafer over 23%. In *26th European Photovoltaic Solar Energy Conference and Exhibition*, 871–874 (EU PVSEC, 2011).
5. Green, M. A., Emery, K., Hishikawa, Y., Warta, W. & Dunlop, D. Solar cell efficiency tables (version 42). *Prog. Photovolt Res. Appl.* **21**, 827–837 (2013).
6. Taguchi, M., Yano, A., Tohoda, S., Matsuyama, K. & Maruyama, E. 24.7% record efficiency HIT solar cell on thin silicon wafer. *IEEE J. Photovolt.* **4**, 96–99 (2014).
7. Masuko, K. et al. Achievement of more than 25% conversion efficiency with crystalline silicon heterojunction solar cell. *IEEE J. Photovolt.* **4**, 1433–1435 (2014).
8. Smith, D. D. et al. Toward the practical limits of silicon solar cells. *IEEE J. Photovolt.* **4**, 1465–1469 (2014).
9. Green, M. A., Emery, K., Hishikawa, Y., Warta, W. & Dunlop, D. Solar cell efficiency tables (version 48). *Prog. Photovolt Res. Appl.* **24**, 905–913 (2016).
10. Green, M. A., Emery, K., Hishikawa, Y., Warta, W. & Dunlop, D. Solar cell efficiency tables (version 49). *Prog. Photovolt Res. Appl.* **25**, 3–13 (2017).
11. Yoshikawa, K. et al. Silicon heterojunction solar cell with interdigitated back contacts for a photoconversion efficiency over 26%. *Nat. Energy* **2**, 17032 (2017).
12. Green, M. A. et al. Solar cell efficiency tables (version 50). *Prog. Photovolt Res. Appl.* **25**, 668–676 (2017).
13. Lin, H. et al. Silicon heterojunction solar cells with up to 26.81% efficiency achieved by electrically optimized nanocrystalline-silicon hole contact layers. *Nat. Energy* **8**, 789–799 (2023).
14. Green, M. A. et al. Solar cell efficiency tables (Version 61). *Prog. Photovolt. Res. Appl.* **31**, 3–16 (2022).

15. Green, M. A. et al. Solar cell efficiency tables (version 65). *Prog. Photovolt Res. Appl.* **33**, 3–15 (2025).
16. Yu, C. et al. Industrial-scale deposition of nanocrystalline silicon oxide for 26.4%-efficient silicon heterojunction solar cells with copper electrodes. *Nat. Energy* **8**, 1375–1385 (2023).
17. Yu, C. et al. Silicon solar cell with undoped tin oxide transparent electrode. *Nat. Energy* **8**, 1119–1125 (2023).
18. Yu, C. et al. 26.6%-efficiency silicon heterojunction solar cell with high-quality cerium and hydrogen codoped indium oxide transparent electrode. *ACS Energy Lett.* **10**, 2503–2511 (2025).
19. Yuan, Y. et al. Study on the process of hydrogen-doped indium oxide for silicon heterojunction solar cell mass production. *Sol. Energy Mater. Sol.Cells* **271**, 112836 (2024).
20. Wang, G. et al. 27.09%-efficiency silicon heterojunction back contact solar cell and going beyond. *Nat. Commun.* **15**, 8931 (2024).
21. Kabayashi, E. et al. Increasing the efficiency of silicon heterojunction solar cells and modules by light soaking. *Sol. Energy Mater. Sol. Cells* **173**, 43–49 (2017).
22. Caputo, D. Degradation and annealing of amorphous silicon solar cells by current injection experiment and modelling. *Sol. Energy Mater. Sol. Cells* **59**, 289–298 (1999).
23. Green, M. A. et al. Solar cell efficiency tables (version 64). *Prog. Photovolt Res. Appl.* **32**, 425–441 (2024).
24. Taguchi, M. et al. An approach for the higher efficiency in the HIT cells. In *Proc. Thirty-first IEEE Photovoltaic Specialists Conference*, 866–871 (IEEE, 2005).
25. Richter, M. et al. A novel approach for single side wet chemical polishing of crystalline silicon solar cells. In *Proc. 28th European Photovoltaic Solar Energy Conference and Exhibition* (2013).
26. Schwab, C. et al. Recombination and optical properties of wet chemically polished thermal oxide passivated Si surfaces. *IEEE J. Photovolt.* **3**, 613–620 (2013).
27. Zielke, D. et al. 21.7% Efficient PERC solar cells with AlOx tunneling layer. In *Proc. 26th European Photovoltaic Solar Energy Conference and Exhibition*, 1115–1119 (EU PVSEC, 2011).
28. Kästner, G. et al. Single side polish etching for the rear side of crystalline silicon wafers. In *Proc. 25th European Photovoltaic Solar Energy Conference and Exhibition*, 6–10 (EU PVSEC, 2010).
29. Horzel, J. et al. Development of rear side polishing adapted to advanced solar cell concepts. In *Proc. 26th European Photovoltaic Solar Energy Conference and Exhibition*, 2010–2016 (EU PVSEC, 2011).
30. Kranz, C. et al. Impact of the rear surface roughness on industrial-type PERC solar cells. In *Proc. 27th European Photovoltaic Solar Energy Conference and Exhibition*, 557–560 (EU PVSEC, 2012).
31. Queisser, S. et al. Inline single side polishing and junction isolation for rear side passivated solar cells. In *Proc. 24th European Photovoltaic Solar Energy Conference and Exhibition*, 1792 (EU PVSEC, 2009).
32. Liu, Z., Sahraei, N., Hoex, B., Aberle, A. G. & Peters, I. M. Optical modelling of alkaline saw-damage-etched rear surfaces of monocrystalline. *IEEE J. Photovolt.* **4**, 1436–1444 (2014).
33. Wang, J., Venkataraj, S., Battaglia, C., Vayalakkara, P. & Aberle, A. G. Analysis of optical and morphological properties of aluminum induced texture glass superstrates. *Jpn. J. Appl. Phys.* **51**, 10NB08 (2012).
34. Umishio, H. et al. Nanocrystalline-silicon hole contact layers enabling efficiency improvement of silicon heterojunction solar cells: impact of nanostructure evolution on solar cell performance. *Prog. Photovolt.* **29**, 344–356 (2021).
35. Lei, C. et al. Phosphorus treatment to promote crystallinity of the microcrystalline silicon front contact layer for highly efficient heterojunction solar cells. *Sol. Energy Mater. Sol. Cells* **209**, 110439 (2020).
36. Mazzarella, L. et al. Nanocrystalline n-type silicon oxide front contacts for silicon heterojunction solar cells: photocurrent enhancement on planar and textured substrates. *IEEE J. Photovolt.* **8**, 70–78 (2018).
37. Hamma, S. & Cabarrocas, P. R. In situ correlation between the optical and electrical properties of thin intrinsic and n-type microcrystalline silicon films. *J. Appl. Phys.* **81**, 7282–7288 (1997).
38. Xia, H. et al. Phonon mode study of Si nanocrystals using micro-Raman spectroscopy. *J. Appl. Phys.* **78**, 6705–6708 (1995).
39. Zhang, S. et al. The diphasic nc-Si/a-Si:H thin film with improved medium-range order. *J. Non Cryst. Solids* **338**, 188–191 (2004).
40. Wei, W., Xu, G., Wang, J. & Wang, T. Raman spectra of intrinsic and doped hydrogenated nanocrystalline silicon films. *Vacuum* **81**, 656–662 (2007).
41. Cabarrocas, P. R., Layadi, N., Heitz, T. & Drevillon, B. Sustrate selectivity in the formation of microcrystalline silicon: Mechanics and technological consequences. *Appl. Phys. Lett.* **66**, 3609–3611 (1995).
42. Kane, D. E. & Swanson, R. M., Measurement of the emitter saturation current by a contactless photoconductivity decay method. In *Proc. IEEE Photovoltaic Specialists Conference* 18, (IEEE, 1985).
43. Schroder, D. K. Carrier lifetimes in silicon. *IEEE Trans. Electron Dev.* **44**, 160–170 (1997).
44. Schmidt, J. Measurement of differential and actual recombination parameters on crystalline silicon wafers [solar cells]. *IEEE Trans. Electron Dev.* **46**, 2018–2025 (1999).
45. Macdonald, D. H. et al. Iron detection in crystalline silicon by carrier lifetime measurements for arbitrary injection and doping. *J. Appl. Phys.* **95**, 1021–1028 (2004).
46. Papet, P. et al. New cell metallization patterns for heterojunction solar cells interconnected by the Smart Wire Connection Technology. *Energy Procedia* **67**, 203–209 (2015).
47. Söderström, T., Papet, P., Yao, Y. & Ufheil, J. Smartwire Connection Technology. In *Proc. 28th European Photovoltaic Solar Energy Conference,* 495–499 (EU PVSEC, 2013).
48. Edwards, M. et al. High efficiency with almost no metallization: multiple busbar wire interconnection of plated solar cells. In *Proc. 28th European Photovoltaics Solar Energy Conference*, 2097–2102 (EU PVSEC, 2013).
49. Zhang, S. et al. Research progress of zero-busbar technology based on heterojunction photovoltaic modules. *Appl. Sci.* **14**, 10845 (2024).
50. Morad, R. et al. Shingled solar cell module: US, US9397252B2[P]. 2017-10-3.
51. Heng, J. B., Rive, P. J., Xie, Z. G. & Yang, B. Cascaded Photovoltaic Structures with Interdigitated Back Contacts: US, US9960302B1[P]. 2018-05-01.
52. Reeves, G. K. & Harrison, H. B. Obtaining the specific contact resistance from transmission line model measurements. *IEEE Electron Dev. Lett.* **3**, 111–113 (2005).
53. Cox, R. H. et al. Ohmic contacts for GaAs devices. *Solid State Electron* **10**, 1213–1218 (1966).
54. Wang, W. et al. An expanded Cox and Strack method for precise extraction of specific contact resistance of transition metal oxide/n-silicon heterojunction. *IEEE J. Photovolt.* **9**, 1113–1120 (2019).
55. Chen, L. et al. Realization of a general method for extracting specific contact resistance of silicon-based dopant-free heterojunctions. *Sol. RRL* **6**, 2100394 (2021).
56. Green, M. A. Solar cell efficiency tables (version 66). *Prog. Photovolt Res. Appl.* **33**, 795–810 (2025).
57. Singh, J. P. et al. Bifacial solar cell measurements under standard test conditions and the impact on cell-to-module loss analysis. *Jpn. J. Appl. Phys.* **56**, 08MD04 (2017).

58. Wong, J. et al. Voltage loss analysis for bifacial silicon solar cells: case for two-dimensional large-area modelling. *IEEE J. Photovolt.* **6**, 1421–1426 (2016).
59. Fell, A. et al. 3-D simulation of interdigitated-back-contact silicon solar cells with quokka including perimeter losses. *IEEE J. Photovolt.* **4**, 1040–1045 (2014).
60. Fell, A. & Altermatt, P. P. A detailed full-cell model of a 2018 commercial PERC solar cell in Quokka3. *IEEE J. Photovolt.* **8**, 1443–1448 (2018).
61. Shockley, W. & Read, W. T. Statistics of the recombinations of holes and electrons. *Phys. Rev.* **87**, 835–842 (1952).

Acknowledgements

This work was financially supported by the National Key R&D Program of China (G.Y., Z.M., and H. Li from Grant No. 2022YFB4200103) and the Basic Research Program of Jiangsu (G.Y. from Grant No. BK20231191).

Author contributions

Z.X. designed the experiments, wrote the manuscript, and was responsible for the simulation. H. Lu, G.Y., Z.G., K.Z., Y.W., Z.M., C.G., H.P., Q.J., and H.Li. were involved in cell engineering and improvement. S.Z., H.C., and X.C. worked on module engineering and improvement. Y.C. and J.G. set the research and development plan and provided technical guidance. All the authors provided feedback and comments.

Competing interests

The authors declare no competing interests.

Additional information

Supplementary information The online version contains supplementary material available at https://doi.org/10.1038/s41467-025-64465-0.

Correspondence and requests for materials should be addressed to Zhigang Xie, Yifeng Chen or Jifan Gao.

Peer review information *Nature Communications* thanks Zengguang Huang, Dongdong Li, Martin Green, Jessica Yajie Jiang, and the other, anonymous, reviewer(s) for their contribution to the peer review of this work. A peer review file is available.